Modelling mooring line snap loads using a high-order finite-volume approach

A.F.L. Governo, J.C.C. Henriques [*], L.M.C. Gato

IDMEC, Instituto Superior Técnico, Universidade de Lisboa, Av. Rovisco Pais 1, 1049-001 Lisboa, Portugal

ARTICLE INFO

ABSTRACT

Wave energy converters' mooring systems are subjected to highly dynamic motions responsible for complex loading mechanisms. Snap loads differ from other dynamic load types by the propagation of tension discontinuities along the cable, which can lead to premature mooring failures if not correctly predicted. Accurate prediction of these loads requires numerical models that can resolve non-smooth solutions. This work developed a (conservative) finite-volume formulation for solving the hyperbolic cable dynamics equation by applying the high-order non-oscillatory central-upwind scheme to calculate the numerical fluxes at the cell interfaces. The central-upwind scheme is a variant of the Godunov-type central finite-volume method and does not need a Riemann solver. This new numerical formulation was tested against analytical and experimental data for a single catenary model under snap-loading conditions. It is shown the method's ability to simulate snap loads correctly, predicting motions and tensions. Furthermore, it exhibits second-order accuracy in space for smooth solutions. This approach is highly robust (with a numerical dissipation independent of the time step) and simpler to implement compared to other codes in the literature.

1. Introduction

Marine cables are prevalent elements in the offshore industry, typically linking a floating device to a submerged device or fixed anchoring system. Examples include towing, instrumentation deployment, tension leg platforms and moorings. For a wave energy converter (WEC) exposed to environmental forces from the ocean, wind and tides, the mooring system acts as a restoring force mechanism while controlling the position and stability of the device. More often than not, mooring cables are the only connecting element, and thus, the technological reliability of a WEC is bounded by the mooring system's mechanical performance (Qiao et al., 2020a).

Most WECs are motion-dependent devices intended to resonate with the incoming waves for increased power generation. This operational mode places complex and nonlinear dynamic loading on the lines. Additionally, because they usually operate in shallow waters with relatively low pre-tensions (Johanning et al., 2006), the cable might become slack and produce transient snap loads during tensioning (Liu, 1973). Snap loads are responsible for sudden large peak dynamic loads, considerably higher than static ones (Niedzwecki and Thampi, 1991). They can be the reason for premature mooring line failure, either by fatigue or overload (Kvitrud, 2014). In this regard, experience from the past shows that cable accidents are not uncommon (Ma et al., 2013) and have strong associations with inaccurate knowledge of actual loading characteristics on the moorings.

The most common dynamic process that leads to snap loading relates to slack conditions on the cable. Slacking is distinguished by local segments where the resultant tension is comparable to the distributed drag force, i.e., a total tension null (Huang and Vassalos, 1993). When the line is slack, the motion at the top induces large hydrodynamic drag forces in the middle of the cable, limiting the velocity while, at the same time, the floating device continues moving at the top (Aranha and Pinto, 2001). Hence, an abrupt retightening occurs and, consequently, a significant increase in the dynamic load. For applications such as floating offshore wind turbines (FOWT) or low-tension tethers, periods of slacking are ordinary since static forces are designed to be small, increasing the risk of snap loads (Hsu et al., 2017; Chen et al., 2018; Koh et al., 1999; Hover, 1997).

Generally, dynamic conditions which can evolve to snap loads involve the sudden application of tensile forces and motions of high excitation frequency or amplitude (Vassalos and Huang, 1996; Qiao et al., 2020b), not necessarily at resonance frequencies (Goeller and Laura, 1971). A mooring line withstands environmental loads with variations of geometry and tension. Tension changes are propagated along the cable through elastic longitudinal waves, and a snap load is a discontinuous (shock) propagation in tension and strain (Palm et al., 2017). Besides cable slacking, a non-smooth tension variation can also appear due to interactions at the touchdown point for catenary

* Corresponding author.
E-mail addresses: andre.governo@tecnico.ulisboa.pt (A.F.L. Governo), joaochenriques@tecnico.ulisboa.pt (J.C.C. Henriques), luis.gato@tecnico.ulisboa.pt (L.M.C. Gato).

Nomenclature

Romans

a	Strain-hardening exponent [-]
A	Area [m^2]
d	Diameter [m]
c	Wave speed [m/s]
C	Coefficient [-]
$\lVert\mathbf{e}\rVert$	Absolute error, Eq. (35)
E	Young's modulus [Pa]
$\mathbf{f}$	Force [N]
$\mathbf{F}$	Flux, Eq. (9)
$\mathbf{F}^*$	Numerical flux, Eq. (28)
I	Cell interval
K_0	Strength coefficient [N]
k_g	Ground stiffness [Pa/m]
L	Cable length [m]
m	Mass [kg]
$\hat{\mathbf{n}}$	Unitary normal vector [-]
N	Number of cells [-]
$\mathbf{r}$	Position [m]
s	Unstretched cable coordinate [m]
$\mathbf{S}$	Source terms vector, Eq. (10)
t	Time [s]
$\mathbf{T}$	Tensile force vector [N]
$\hat{\mathbf{t}}$	Unitary tangential vector [-]
$\mathbf{U}$	Conservative variables vector, Eq. (8)
$\mathbf{v}$	Absolute velocity [m/s]
$\mathbf{w}$	Relative velocity [m/s]
$\mathbf{W}$	Intermediate solution
z	Vertical coordinate [m]

Greek symbols

Δ	Variation, interval
λ	Eigenvalue [-]
$\boldsymbol{\Lambda}$	Eigenvalues vector [-]
μ	Dynamic friction coefficient [-]
ε	Strain [-]
ξ	Damping ratio [-]
ρ	Density [kg/m^3]
τ	Period [s]

Superscripts

$-$	Average quantity
$\sim$	Reconstructed quantity
$\cdot$	Time derivative
num	Numerical value
exact	Analytical solution value

Subscripts

0	Initial conditions
a	Added mass
b	Buoyancy
c	Cable
d	Drag
f	Final
g	Ground
max	Maximum
n	Normal
ref	Reflected
sh	Shock
t	Tangential
w	Water
z	Vertical projection

Acronyms

CFL	Courant–Friedrichs–Lewy
FOWT	Floating Offshore Wind Turbines
FVM	Finite-Volume Method
IVP	Initial-Value Problem
MWL	Mean Wave Line
ODE	Ordinary Differential Equations
PDE	Partial Differential Equations
TVD	Total Variation Diminishing
WEC	Wave Energy Converter

moorings (Gobat and Grosenbaugh, 2001), and nonlinear constitutive laws of synthetic materials (Tjavaras, 1996). Gobat and Grosenbaugh (2001) define a criterion for snap events based on the ratio between the velocity at the touchdown point and the transverse wave velocity. Derivations of similar criteria are also presented in (Niedzwecki and Thampi, 1991), (Suhara et al., 1981) and (Hann, 1995).

Over the years, an adequate effort has been devoted to investigating snap loading in mooring cables from both the numerical and experimental sides. Relevant experimental studies on mooring cables used in FOWT (Hsu et al., 2017; Masciola et al., 2013; Azcona et al., 2017) and WECs (Savin et al., 2012; Hennessey et al., 2005) are reported in the literature, along with other situational applications. A generic overview can be found in (Hsu et al., 2014). However, difficulties in obtaining accurate experimental measurements were identified (Harnois, 2014). Additionally, model testing is often unfeasible due to dynamic dissimilarities and cost (Bergdahl et al., 2016). This issue raises the importance of accurate numerical models that capture dynamic behaviour and snap loads.

Many numerical modelling tools exist for mooring lines, but only a few are targeted to handle snap loading and slacking regimes. An extensive review of these numerical tools applied in WEC moorings can be found in (Davidson and Ringwood, 2017). Vassalos and Kourouklis (1998) compare experimental results for different model tests with a lumped mass method that allows bilinear axial stiffness materials. When the cable is slack, non-compressive springs are used to simulate the loss of axial stiffness. Their numerical model presents a good agreement for smooth motions but substantially underpredicts the maximum tension at large amplitudes and frequencies during slack-taut states.

Despite these efforts, numerical methods suitable to capture discontinuities in tension are needed. Appropriate techniques should resolve the longitudinal and transverse waves accurately. On this matter, a high-order Local Discontinuous Galerkin method was developed for the hyperbolic numerical cable equation formulated in conservative form (Palm et al., 2017). The solutions are allowed to be discontinuous over the element boundaries with a Lax–Friedrichs type of flux to solve
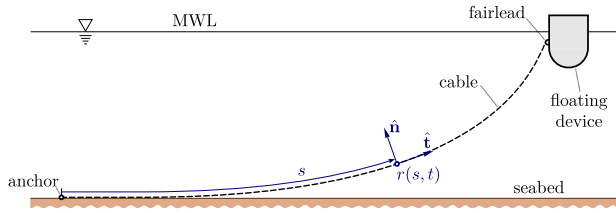
Fig. 1. Coordinate system for the mooring cable on a inertial frame of reference (fixed at the anchor point).

the local Riemann problem. Good agreement was obtained by comparing with model testing results for a catenary chain from (Bergdahl et al., 2016). Their formulation can include bending stiffness by adding a shear force vector term to the moment balance equation (Palm and Eskilsson, 2020). The key feature of their work relies on the use of high-resolution shock-capturing techniques borrowed from the finite-volume framework, which can handle solution discontinuities. Additionally, by using the conservative formulation for the hyperbolic cable dynamics partial differential equations (PDE), physically correct wave speeds of propagation and weak form solutions are obtained (LeVeque, 1990; Lax and Wendroff, 1960; Hou and Floch, 1994).

This paper presents a new approach, based on a Finite Volume Method (FVM), for solving the hyperbolic system of PDEs governing the dynamic cable equations. The method solves the flux term of the equations through a Godunov-type central-upwind scheme (Kurganov et al., 2001). Discontinuities are permitted in the solution while preserving the best features of a Godunov finite-volume framework, namely simplicity and avoidance of Riemann solvers. This scheme's numerical dissipation is independent of the time resolution and is of the order of $\mathcal{O}[\Delta s^2]$, even in the semi-discrete version (s denotes the spatial coordinate). The semi-discrete version can be directly evolved in time by stable integration schemes such as the Runge–Kutta.

From the present work, the most relevant contributions can be summarized in the following topics:

- Development of a new numerical scheme for simulating the dynamics of perfectly flexible mooring cables based on a finite-volume framework (central-upwind scheme). The scheme is especially suited to handle discontinuities in the solution, thus adapted for snap load and slacking regimes.
- Comparison of the numerical scheme results against suitable analytical and experimental case tests.

The paper's structure is as follows. Section 2 presents the governing equations for the cable dynamics problem written in the conservative form and the necessary assumptions required for their calculation. Next, the numerical formulation for the system of hyperbolic PDEs is developed based on the central-upwind scheme. Numerical results of the newly developed scheme in selected validation cases are presented in Section 3, while conclusions appear in Section 4.

2. Numerical modelling

2.1. Cable equations

For practical wave energy applications, the mooring line is slender since its length is several orders of magnitude greater than the diameter. Consequently, the three-dimensional motion is approximated by the motion of the mooring centreline. Let us define the local centreline coordinate $s \in [0, L]$ as the unstretched length along the cable of length L and denote $\mathbf{r}(s,t) \in \mathbb{R}^3$ as the position vector at time t, in accordance with Fig. 1. Moreover, at each point, the cable orientation is given by the unit tangential vector $\hat{\mathbf{t}}$:

$$\hat{\mathbf{t}} = \frac{\partial \mathbf{r}}{\partial s} \left\| \frac{\partial \mathbf{r}}{\partial s} \right\|^{-1}. \tag{1}$$

Here, $\| \cdot \|$ denotes the Euclidean norm. Following a derivation in an inertial frame of reference, the dynamics of a single mooring cable is dictated by the following equation of motion (Aamo and Fossen, 2000, 2001)

$$m_c \frac{\partial^2 \mathbf{r}}{\partial t^2} = \frac{\partial \mathbf{T}}{\partial s} + (1 + \varepsilon)\mathbf{f}, \tag{2}$$

which considers the balance of forces on a cable segment. In Eq. (1), m_c is the mass of cable per unit of unstretched length, $\mathbf{T}$ is the tensile force vector, ε is the strain and $\mathbf{f}$ is the external force vector. The tensile force vector $\mathbf{T}$ acting on the cable segment can be divided into a tangential $\mathbf{T}_t$ component and a normal $\mathbf{T}_n$ component:

$$\mathbf{T} = \mathbf{T}_t + \mathbf{T}_n, \tag{3}$$

where $\mathbf{T}_t = T\hat{\mathbf{t}}$. The magnitude of the tangential force T depends on the constitutive law of the material and is a functional relation of the strain (and strain rate), meaning: $T = T(\varepsilon, \dot{\varepsilon})$. The strain on the cable centreline is measured according to:

$$\varepsilon = \left\| \frac{\partial \mathbf{r}}{\partial s} \right\| - 1. \tag{4}$$

On the other hand, the normal component $\mathbf{T}_n$ represents the shear forces acting on the cable and can be computed with some simplifying assumptions (see Triantafyllou, 1999; Palm and Eskilsson, 2020). In the absence of bending stiffness and torsional stiffness, the internal moment vector is zero and, thus, $\mathbf{T}_n = 0$. This is a common approach for solving the equations and is suitable for most cable materials, such as chains, under normal sea conditions. However, one needs to be attentive when the tension is close to zero since there is no restoring mechanism apart from axial stiffness, and the problem becomes ill-posed (Triantafyllou and Howell, 1994).

A stress–strain relation is needed to evaluate the tension magnitude T at each cable point and close the system of equations. Here, a linear elastic response was applied by using Hooke's law

$$T = EA_c \max(\varepsilon, 0), \tag{5}$$

where E is the Young's modulus of the material and A_c is the unstretched area of the cable. The stress–strain equation is, therefore, only dependent on the strain ε at each cell and does not depend on the strain rate $\dot{\varepsilon}$. Note that negative strain values are not allowed since it would mean the cable segment is under compression.

The equation of motion can be written as a system of first-order partial differential equations if we notice that $\mathbf{v} = \partial \mathbf{r}/\partial t$ and by defining the variable $\mathbf{q} = \partial \mathbf{r}/\partial s$. It is then possible to solve the assembled system as a conservation law with a source term when the original form of Eq. (2) is retained. Additionally, the position of the cable $\mathbf{r}(s,t)$ is a continuous and differentiable function. Hence,

$$\frac{\partial \mathbf{q}}{\partial t} = \frac{\partial \mathbf{v}}{\partial s}. \tag{6}$$

With the compatibility relation (Eq. (6)), the final form of the system of equations governing the cable dynamics is

$$\frac{\partial \mathbf{U}}{\partial t} = \frac{\partial \mathbf{F}}{\partial s} + \mathbf{S}, \tag{7}$$

and the conserved variables $\mathbf{U}$, fluxes $\mathbf{F}$ and source terms $\mathbf{S}$ are defined as

$$\mathbf{U} = \begin{pmatrix} m_c \mathbf{v} \\ \mathbf{q} \end{pmatrix}, \tag{8}$$

$$\mathbf{F}(\mathbf{U}) = \begin{pmatrix} \mathbf{T} \\ \mathbf{v} \end{pmatrix}, \tag{9}$$

and

$$\mathbf{S}(\mathbf{U}) = \begin{pmatrix} (1 + \varepsilon)\mathbf{f} \\ \mathbf{0} \end{pmatrix}. \tag{10}$$

The vector $\mathbf{f}$ contains all external loads per unit length exerted on the cable by the environment, namely:

$$\mathbf{f} = \mathbf{f}_b + \mathbf{f}_a + \mathbf{f}_D + \mathbf{f}_g. \tag{11}$$

Here, $\mathbf{f}_b$ are the buoyancy and weight forces, $\mathbf{f}_a$ are the added mass and Froude–Krylov forces, $\mathbf{f}_D$ are the drag forces and $\mathbf{f}_g$ are the ground forces (when the cable is in contact with the sea bottom).

The net result of the weight and buoyancy forces acting at each node can be combined into what is called the submerged weight $\mathbf{f}_b$ and is given by

$$\mathbf{f}_b = \frac{m_c}{1+\varepsilon} \left(1 - \frac{\rho_w}{\rho_c} \right) \mathbf{g}, \tag{12}$$

where ρ_w and ρ_c are the densities of water and cable material, respectively, and $\mathbf{g}$ is the gravity acceleration. This force always acts vertically on the cable (considering a global frame of reference), and its direction depends on the ratio of the density terms.

Hydrodynamic loads exerted on the cable are due to the relative motion between the cable and the surrounding fluid and are estimated using the Morison equation. These loads are typically decomposed into the hydrodynamic added mass force $\mathbf{f}_a$ and the hydrodynamic drag force $\mathbf{f}_D$, calculated from

$$\mathbf{f}_a = \frac{1}{4} \rho_w \frac{\pi d_c^2}{(1+\varepsilon)} \left(C_{a_t} \dot{\mathbf{w}} \cdot \hat{\mathbf{t}} + C_{a_n} \dot{\mathbf{w}} \cdot \hat{\mathbf{n}} + \dot{\mathbf{v}}_w \right), \tag{13}$$

where C_{a_t} and C_{a_n} are the non-dimensional coefficients of added mass in the tangential and normal directions, respectively, and d_c is the unstretched diameter of the cable. Note that this force is dependent on the surrounding water velocity $\mathbf{v}_w$ (if current exists), either directly or indirectly through the relative velocity of the cable $\mathbf{w} = \mathbf{v}_w - \mathbf{v}$. The drag force $\mathbf{f}_D$ is calculated through

$$\mathbf{f}_D = \frac{1}{2} \frac{\rho_w d_c}{\sqrt{1+\varepsilon}} \left(C_{D_t} \mathbf{w} \cdot \hat{\mathbf{t}} \|\mathbf{w} \cdot \hat{\mathbf{t}}\| + C_{D_n} \mathbf{w} \cdot \hat{\mathbf{n}} \|\mathbf{w} \cdot \hat{\mathbf{n}}\| \right). \tag{14}$$

The interactions between the sea bottom and the cable are accounted for by using a linear stiffness spring–damper model for the vertical force $\mathbf{f}_{g_n}$, while a tangential friction model $\mathbf{f}_{g_n}$ is applied when horizontal velocities are present,

$$\mathbf{f}_{g_n} = k_g d_c \left(z_g - r_z \right) - 2\xi_g \sqrt{k_g m_c d_c} \min\left(\mathbf{v} \cdot \hat{\mathbf{n}}, 0 \right), \tag{15}$$

$$\mathbf{f}_{g_t} = \operatorname{sgn}\left(\mathbf{v} \cdot \hat{\mathbf{t}} \right) \mu_g \tanh\left(\frac{\pi}{v_\mu} \mathbf{v} \cdot \hat{\mathbf{t}} \right) \mathbf{f}_b, \tag{16}$$

where k_g is the spring stiffness, ξ_g is the damping ratio, μ_g is the dynamic friction coefficient corresponding to a maximum friction velocity v_μ, and sgn is the signum function. The model is applied whenever the vertical coordinate of a node r_z is in contact or below the sea bottom vertical coordinate z_g ($z_g \geq r_z$). Moreover, the damping force part is activated if and only if the velocity of a ground node is negative (i.e., it is moving towards the sea bottom).

2.2. Numerical formulation

Let us consider the system of nonlinear hyperbolic partial differential equations written in a canonical conservative form:

$$\frac{\partial \mathbf{U}}{\partial t} + \frac{\partial \mathbf{F}}{\partial s} = \mathbf{0}, \tag{17}$$

where $\mathbf{U}(s,t)$ is a vector of conserved quantities and $\mathbf{F}(\mathbf{U})$ is a nonlinear flux, subjected to a given initial condition $\mathbf{U}(s,0) = \mathbf{U}_0(s)$ and appropriate boundary conditions. Initial value problems (IVPs) of the general form of Eq. (17) are prone to develop discontinuities such as shocks even if the initial data is smooth. Hence, high-resolution and non-oscillatory numerical schemes are needed.

The system of Eqs. (17) is hyperbolic if the Jacobian $\partial \mathbf{F}/\partial \mathbf{U}$ has real eigenvalues. Applying a similarity transformation to $\partial \mathbf{F}/\partial \mathbf{U}$ the following eigenvalue matrix is obtained

$$\Lambda = \operatorname{diag}\left(-c_n \quad -c_n \quad c_n \quad c_n \quad -c_t \quad c_t \right), \tag{18}$$

where

$$c_t = \sqrt{\frac{1}{m_c} \frac{\partial T}{\partial \varepsilon}}, \tag{19}$$

$$c_n = \sqrt{\frac{T}{m_c \|\mathbf{q}\|}},$$

are the normal and tangential wave velocities propagating in the cable. Consequently, the system is hyperbolic if the tension (or its derivative) is always positive and different than zero (Cristescu, 2007).

Explicit numerical schemes are used to capture such discontinuities in this type of hyperbolic equation, including mooring cable equations. Tjavaras (1996) studied shock formation in mooring lines by using the well-known Lax–Friedrichs scheme (Tjavaras, 1996; Lax, 1954). However, this scheme lacks resolution, and it is required to satisfy the CFL condition with significant restrictions in terms of time step. Moreover, the amount of numerical dissipation accumulated is of order $\mathcal{O}[(\Delta s)^{2r}/\Delta t]$, with r as the formal order of the scheme, making it prohibitive for long simulations. Finally, it is not formulated in the conservative form. Hence, if a shock occurs, the numerical solution may be incorrect.

2.3. Central-upwind scheme

A short description of the fundamentals of finite-volume methods and, particularly, central-upwind schemes, is provided in this section. The complete derivation is sourced to (Kurganov et al., 2001).

Consider the one-dimensional hyperbolic system of Eqs. (17) to be solved on a computational domain divided by uniform and non-overlapping finite-volume cells defined by the intervals $I_i = \left[s_{i-\frac{1}{2}}, s_{i+\frac{1}{2}} \right]$, with $i = 1, \ldots, N$. Here N is the number of cells. The discrete cell solution $\overline{\mathbf{U}}_i$ can be approximated by averaging the exact solution $\mathbf{U}_i$ over I_i

$$\overline{\mathbf{U}}_i(t) = \frac{1}{\Delta s} \int_{I_i} \mathbf{U}(s,t) \; ds, \tag{20}$$

where $\Delta s = s_{i+\frac{1}{2}} - s_{i-\frac{1}{2}}$. The idea of the FV method is to obtain an algebraic equation for all $\mathbf{U}_i$ by simply writing the conservation law in each cell I_i. For a one-dimensional space, integrating Eq. (17) in all cells and integrating the flux by parts we get

$$\frac{\partial}{\partial t} \int_{I_i} \mathbf{U}(s,t) ds + \left(\mathbf{F}(\mathbf{U}(s,t)) \right) \Big|_{s_{i-\frac{1}{2}}}^{s_{i+\frac{1}{2}}} = 0. \tag{21}$$

Since FV schemes are developed under the integral (also called weak) formulation, Eq. (21), they preserve their validity even for piecewise smooth solutions and are, therefore, appropriate to simulate discontinuous solutions of the nonlinear hyperbolic system of equations. Note that Eq. (20) can be exactly substituted into Eq. (21), yielding

$$\frac{d}{dt} \overline{\mathbf{U}}_i(t) = -\frac{1}{\Delta s} \left(\mathbf{F}^*_{i+\frac{1}{2}}(t) - \mathbf{F}^*_{i-\frac{1}{2}}(t) \right), \tag{22}$$

where $\mathbf{F}^*$ is a consistent numerical flux at the cell interfaces $s_{i+\frac{1}{2}}$. Typically, this flux is evaluated approximately, by solving a local Riemann problem. Consequently, the approximation results from the flux discretization. Moreover, since only cell averages are known, a solution reconstruction at the cell interface is needed to compute the numerical fluxes. This reconstruction makes use of the cell averages of neighbouring cells.

Assuming the cell average values $\overline{\mathbf{U}}_i$ are available at a certain time t^n, a conservative piecewise linear interpolant $\tilde{\mathbf{U}}_i$ can be reconstructed for all $s \in I_i$, of the form

$$\tilde{\mathbf{U}}_i^n = \overline{\mathbf{U}}_i^n + (s - s_i) \left(\mathbf{U}_s \right)_i^n. \tag{23}$$

Note that the scheme's formal order of (spatial) accuracy is determined by the polynomial interpolant order. In this case, the discrete numerical derivatives $\left(\mathbf{U}_s \right)_i^n$ are, at least, a first-order approximation of the slope
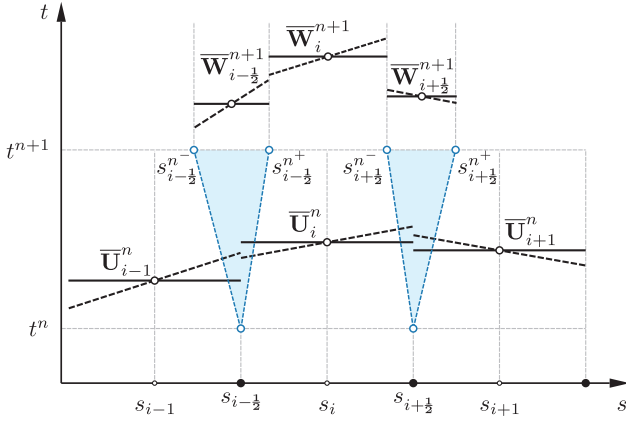
Fig. 2. Reconstruction and evolution of the cell average solutions. Adaptive space–time control volumes according to the Riemann fan size are used for evolving the solution in time on a intermediate grid (Kurganov et al., 2001).

and, thus, the scheme is second-order accurate (Kurganov et al., 2001). Additionally, if the numerical slopes are to be computed using total variation diminishing (TVD) approaches – e.g., nonlinear limiters – the reconstruction is essentially non-oscillatory (Kurganov and Tadmor, 2000).

In the present work, the first-order approximate derivatives $(\mathbf{U}_s)_i$ are calculated using the generalized minmod limiter

$$(\mathbf{U}_s)_i = \text{minmod}\left(\theta\frac{\mathbf{U}_i - \mathbf{U}_{i-1}}{\Delta s}, \frac{\mathbf{U}_{i+1} - \mathbf{U}_{i-1}}{2\Delta s}, \theta\frac{\mathbf{U}_{i+1} - \mathbf{U}_i}{\Delta s}\right), \quad (24)$$

where $1 \le \theta \le 2$ controls the reconstruction sharpness. A $\theta = 2$ was employed in this work. The value of $\theta = 1$ corresponds to this limiter's more diffusive (but less oscillatory) version. The minmod function is defined as

$$\text{minmod}(x_k) = \begin{cases} \min\{x_k\}, & \text{if } x_k > 0 \quad \forall k, \\ \max\{x_k\}, & \text{if } x_k < 0 \quad \forall k, \\ 0, & \text{otherwise.} \end{cases} \quad (25)$$

The application of Eq. (23) provides the values of the cell interfaces $s = s_{i+\frac{1}{2}}$ from the cell averages, which are, in general, discontinuous. However, these discontinuities propagate with finite speeds due to the hyperbolicity of the equations, and the one-sided local propagation speeds determine the size of the Riemann fans. These speeds, here denoted by $c_{i+\frac{1}{2}}^{\pm}$, are estimated by the maximum and minimum eigenvalues $\lambda_1 < \cdots < \lambda_N$ of the flux Jacobian matrix $\partial \mathbf{F}(\mathbf{U})/\partial \mathbf{U}$ at $s = s_{i+\frac{1}{2}}$ (Kurganov et al., 2001),

$$c_{i+\frac{1}{2}}^{+} = \max\left(\lambda_N\left(\mathbf{U}_{i+\frac{1}{2}}^{-}\right), \lambda_N\left(\mathbf{U}_{i+\frac{1}{2}}^{+}\right), 0\right),$$
$$c_{i+\frac{1}{2}}^{-} = \min\left(\lambda_1\left(\mathbf{U}_{i+\frac{1}{2}}^{-}\right), \lambda_1\left(\mathbf{U}_{i+\frac{1}{2}}^{+}\right), 0\right). \quad (26)$$

This suggests adaptively splitting the space–time control volumes into smooth and non-smooth regions, depending on the size of the Riemann fans at each cell interface (see Fig. 2), and evolving the solutions accordingly. Concretely, the solution of the equations may only be discontinuous inside the space–time control volume defined by $\left[s_{i+\frac{1}{2}}^{n-}, s_{i+\frac{1}{2}}^{n+}\right] \times \left[t^n, t^{n+1}\right]$, where $s_{i+\frac{1}{2}}^{n-} = s_{i+\frac{1}{2}} + c_{i+\frac{1}{2}}^{-}\Delta t$, $s_{i+\frac{1}{2}}^{n+} = s_{i+\frac{1}{2}} + c_{i+\frac{1}{2}}^{+}\Delta t$. On the other hand, the smooth solution is contained inside the interval $\left[s_{i-\frac{1}{2}}^{n+}, s_{i+\frac{1}{2}}^{n-}\right] \times \left[t^n, t^{n+1}\right]$. This is a key feature of the central-upwind schemes and ensures no Riemann solvers are necessary.

The solution in the new non-uniform mesh is then evolved in time by integration, producing two intermediate cell averages $\overline{\mathbf{W}}_{i+\frac{1}{2}}^{n+1}$ and $\overline{\mathbf{W}}_{i}^{n+1}$ which are projected into the original grid to compute $\overline{\mathbf{U}}_i^{n+1}$. The projection of $\mathbf{W}$ uses a reconstruction procedure similar to that of $\mathbf{U}$,

that is, realizing the average over the cell,

$$\overline{\mathbf{U}}_i^{n+1} = \frac{1}{\Delta s}\int_{s_{i-\frac{1}{2}}}^{s_{i+\frac{1}{2}}}\left(\widetilde{\mathbf{W}}_{i-\frac{1}{2}}^{n+1}(s) + \widetilde{\mathbf{W}}_{i}^{n+1}(s) + \widetilde{\mathbf{W}}_{i+\frac{1}{2}}^{n+1}(s)\right)\mathrm{d}s. \quad (27)$$

Accordingly, a fully discrete Godunov-type central-upwind scheme is obtained. Moreover, a semi-discrete formulation is possible by taking the limit of $\Delta t \to 0$. The central-upwind scheme in its semi-discretized form assumes the form of Eq. (22) with the following numerical fluxes $\mathbf{F}^*$ (time dependence of the variables is omitted) (Kurganov et al., 2001)

$$\mathbf{F}_{i+\frac{1}{2}}^*(t) = \frac{c_{i+\frac{1}{2}}^+\mathbf{F}\left(\mathbf{U}_{i+\frac{1}{2}}^-\right) - c_{i+\frac{1}{2}}^-\mathbf{F}\left(\mathbf{U}_{i+\frac{1}{2}}^+\right)}{c_{i+\frac{1}{2}}^+ - c_{i+\frac{1}{2}}^-} + \frac{c_{i+\frac{1}{2}}^+ c_{i+\frac{1}{2}}^-}{c_{i+\frac{1}{2}}^+ - c_{i+\frac{1}{2}}^-}\left(\mathbf{U}_{i+\frac{1}{2}}^+ - \mathbf{U}_{i+\frac{1}{2}}^-\right). \quad (28)$$

Here, $\mathbf{U}_{i+\frac{1}{2}}^{\pm}$ correspond to the reconstructed values of the cell interfaces. The final formulation with the source term is

$$\frac{\mathrm{d}}{\mathrm{d}t}\overline{\mathbf{U}}_i(t) = -\frac{\mathbf{F}_{i+\frac{1}{2}}^*(t) - \mathbf{F}_{i-\frac{1}{2}}^*(t)}{\Delta s} - \mathbf{S}_i(t). \quad (29)$$

The system of ODEs is integrated in time with the third-order strong stability preserving Runge–Kutta method (SSP-RK3) to maintain the order of accuracy and stability properties. Assuming $\mathbf{U}^n = \mathbf{L}(\mathbf{U})$ is the approximate solution of the PDE, then

$$\mathbf{U}^{(1)} = \mathbf{U}^n + \Delta t\,\mathbf{L}(\mathbf{U}^n),$$
$$\mathbf{U}^{(2)} = \frac{3}{4}\mathbf{U}^n + \frac{1}{4}\mathbf{U}^{(1)} + \frac{1}{4}\Delta t\,\mathbf{L}(\mathbf{U}^{(1)}), \quad (30)$$
$$\mathbf{U}^{n+1} = \frac{1}{3}\mathbf{U}^n + \frac{2}{3}\mathbf{U}^{(2)} + \frac{2}{3}\Delta t\,\mathbf{L}(\mathbf{U}^{(2)}),$$

where the time step is calculated based on the CFL number,

$$\text{CFL} = \frac{1}{2}\frac{c_{\max}\Delta t}{\Delta s}. \quad (31)$$

The maximum wave speed corresponds to $c_{\max} = \max\left(c_{i+\frac{1}{2}}^+, c_{i+\frac{1}{2}}^-\right)$.

Finally, the boundary conditions on the state variables are enforced on the grid by using ghost cells on the reconstruction approach at the interface edge of the domain. This approach was chosen due to its inherent simplicity (LeVeque, 1990).

3. Validation cases

In this section, the results of the developed numerical formulation are compared with analytical and experimental results available in the literature. Three test cases were selected:

- Taut vibrating string.
- Shock wave propagation in a synthetic cable.
- Dynamics of a catenary mooring.

3.1. Taut vibrating string

The well-known vibrating string problem is the first validation case with an analytical solution. Let us consider a homogeneous string with constant mass (per unit of length) m_c that is axially stretched between two fixed endpoints at the same vertical position. The applied strain ε_0 and tensile force T_0 on the string is, thus, constant in space and time. A simplified form of the cable dynamics equation (Eq. (2)) is derived when small displacements are considered and coincides with the one-dimensional linear wave equation

$$\frac{\partial^2 r}{\partial t^2} = c^2\frac{\partial^2 r}{\partial s^2}, \quad (32)$$

where r corresponds to the vertical displacement. The wave speed in the normal direction c is calculated from

$$c = \sqrt{\frac{T_0}{m_c(1 + \varepsilon_0)}}. \quad (33)$$

For comparison, the same initial conditions as reported in (Palm et al., 2017) are used, that is: unstretched string length $L_0 = 100\,\text{m}$, mass $m_c = $
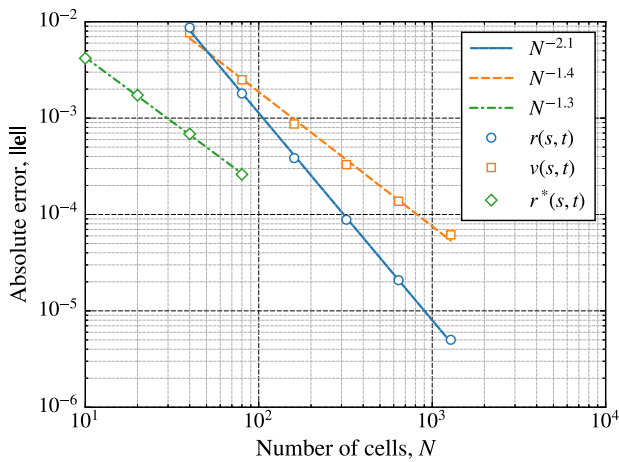
Fig. 3. Absolute error $\|\mathbf{e}\|$ for the vibrating string problem. $\mathbf{r}^*(s,t)$ corresponds to the solution using the hp-adaptive Discontinuous Galerkin method from (Palm et al., 2017).

Table 1
L^2-norm error ($\|\mathbf{e}\|$) for position $\mathbf{r}(s,t)$ and velocity $\mathbf{v}(s,t)$.

N	$\mathbf{r}(s,t)$		$\mathbf{v}(s,t)$	
	$\|\mathbf{e}_1\|$ [m]	Rate	$\|\mathbf{e}_2\|$ [m/s]	Rate
40	8.7×10^{-3}	–	7.7×10^{-3}	–
80	1.8×10^{-3}	2.3	2.5×10^{-3}	1.6
160	3.9×10^{-4}	2.2	8.7×10^{-4}	1.5
320	8.8×10^{-5}	2.1	3.3×10^{-4}	1.4
640	2.1×10^{-5}	2.1	1.4×10^{-4}	1.3
1280	5.0×10^{-6}	2.1	6.2×10^{-5}	1.2

$0.1 \, \mathrm{kg/m}$ and pre-tension force $T_0 = 1100 \, \mathrm{N}$, which is equivalent to an initial strain $\varepsilon_0 = 0.1$. The initial configuration of the string corresponds to $r(s,0) = \sin(\pi s/L_0)$. In these circumstances, the analytical solution to this problem is (Greiner, 2009)

$$r(s,t) = \cos\left(\frac{c\pi}{L_0}t\right)\sin\left(\frac{\pi}{L_0}s\right). \tag{34}$$

The solution obtained by the analytical formula is compared with the numerical one via the L^2-norm of the absolute error $\|\mathbf{e}\|$, after one period of string oscillation,

$$\|\mathbf{e}\| = \sqrt{\frac{1}{N}\sum_{i=1}^{N}\left(\mathbf{U}_i^{\mathrm{num}} - \mathbf{U}_i^{\mathrm{exact}}\right)^2}. \tag{35}$$

The results are shown in Fig. 3 and Table 1, for increasing number of nodes N and CFL = 0.01. Results show excellent agreement with the analytical solution, particularly for the position $\mathbf{r}$ where the numerical scheme exhibits a second-order convergence rate (as expected). Further, for comparison, the solution obtained using the hp-adaptive Discontinuous Galerkin method with $p = 1$ (linear polynomial in each element) from (Palm et al., 2017) is also displayed. Both methods are compared for the same number of degrees of freedom. Although the Discontinuous Galerkin method presents lower values of the error $\|\mathbf{e}\|$ for the same number of degrees of freedom, it has a lower convergence rate (approximately given by $p + \frac{1}{2} = 1.5$) in comparison with the presented central-upwind scheme.

3.2. Shock propagation

This test case analyzes propagating shock conditions on a one-dimensional horizontal cable with a nonlinear constitutive function of the type $T = T(\varepsilon)$. Shock formation, propagation and reflection properties are compared against the analytical solution implemented in (Tjavaras, 1996) with the method of characteristics.

Table 2
Comparison between analytical and numerical results.

Variable	$a = 10$		$a = 20$	
	Analytical	Numerical	Analytical	Numerical
T_{ref} [N]	3053.8	3051.4	13347.7	13311.0
$\varepsilon_{\mathrm{ref}}$ [-]	0.1400	0.1399	0.1332	0.1331

This problem considers a horizontal cable at rest, constituted by a synthetic material with an exponential tension–strain relation of the form

$$T(\varepsilon) = K_0\left(e^{a\varepsilon} - 1\right), \tag{36}$$

where K_0 and a are empirical variables that correspond to a certain material. The cable is excited by a horizontal force $f(t)$ in one end ($s = L$) while it is kept fixed on the other ($s = 0$). Under these conditions, analytical expressions for shock formation, propagation, and reflection are derived (Tjavaras, 1996).

The cable has the following properties: unstretched cable length $L_0 = 800 \, \mathrm{m}$, mass $m_c = 1 \, \mathrm{kg/m}$ and strength coefficient of $K_0 = 1000 \, \mathrm{N}$. Additionally, two different values for the strain-hardening exponent are studied, $a = 10$ and $a = 20$, and a constant initial strain $\varepsilon_0 = 0.05$ is applied.

The horizontal excitation force (or strain) function has the form

$$f(t) = \begin{cases} (\varepsilon_{\mathrm{f}} - \varepsilon_0) \, t/t_{\mathrm{f}} + \varepsilon_0 & \text{for } t < t_{\mathrm{f}} \\ \varepsilon_{\mathrm{f}} & \text{for } t \geq t_{\mathrm{f}} \end{cases}, \tag{37}$$

where the final strain is $\varepsilon_{\mathrm{f}} = 0.1$, achieved at a time $t_{\mathrm{f}} = 1 \, s$.

The wave speed in the tangential direction is calculated from (see Eq. (19))

$$c_{\mathrm{t}}(\varepsilon) = \sqrt{\frac{aK_0}{m_c}e^{a\varepsilon}}. \tag{38}$$

In this case, a shock is formed during tension loading because $c_{\mathrm{t}}(\varepsilon)$ increases with ε. Therefore, under these conditions, a tension discontinuity will be generated after a specified time and reflected at the fixed end of the cable. The strain value after shock reflection is given by (Tjavaras, 1996)

$$\varepsilon_{\mathrm{ref}} = \frac{2\ln\left(2\sqrt{e^{a\varepsilon_{\mathrm{f}}}} - \sqrt{e^{a\varepsilon_0}}\right)}{a}. \tag{39}$$

The numerical formulation can thus be compared with the above equations provided by the method of characteristics. For the numerical setup, a total of $N = 1000$ nodes were utilized in the cable's spatial discretization, with a time step defined by a CFL = 0.5. The results are plotted in Figs. 4 and 5.

Both graphs demonstrate that the increase in tension imposed at the right end induces the formation of a shock after a specified time, as predicted by the analytical solution. This shock is reflected on the fixed left end, with a corresponding augmentation of strain and tension. The variation of the exponent value a introduces a different variation of the wave speed $c_{\mathrm{t}}(\varepsilon)$ as well as different values of tension. For $a = 20$, the tension discontinuity is much more significant. Therefore, achieving perfect shock resolution (with the same number of nodes) is more difficult without small overshooting at the peak.

The analytical values of tension and strain after reflection are compared against the numerical ones in Table 2. A very close agreement is obtained for both values. As such, the shocks have the right propagation and reflection characteristics demonstrating that the numerical formulation is correctly implemented and with a high resolution.

3.3. Catenary mooring

In this subsection, the numerical model is validated using experimental data for a dynamically excited catenary in a water tank
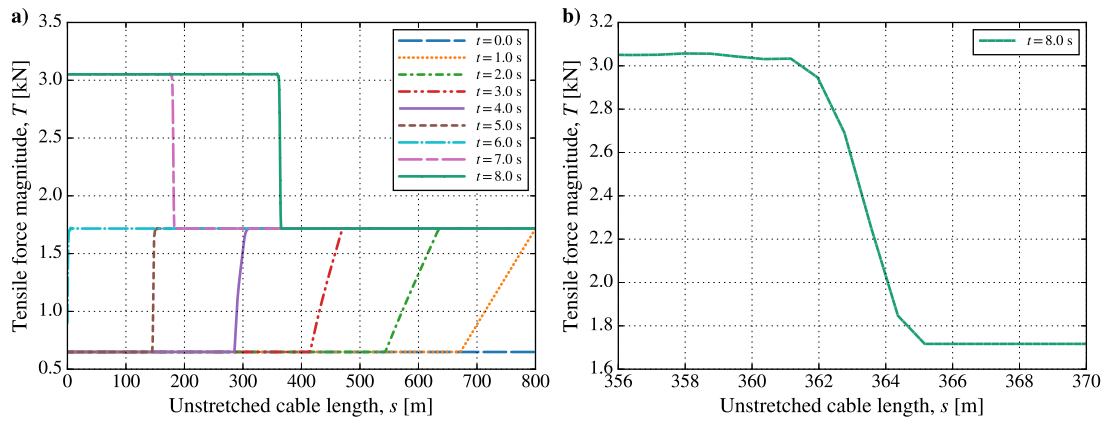
Fig. 4. (a) Evolution of the tension magnitude on the cable over time for a material with $a = 10$. (b) Zoom of shock obtained at $t = 8$ s.
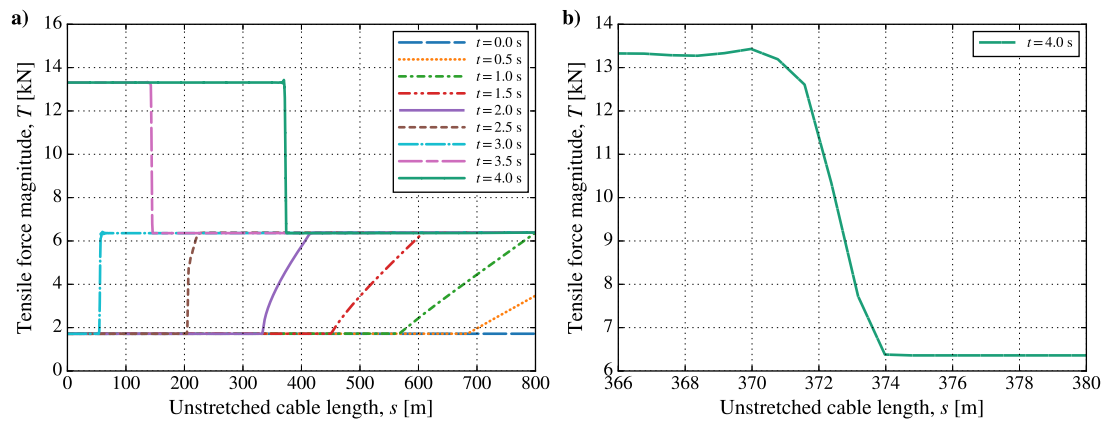

Fig. 5. (a) Evolution of the tension magnitude on the cable over time for a material with $a = 20$. (b) Zoom of shock obtained at $t = 4$ s.
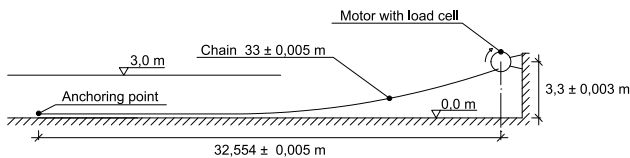

Fig. 6. Schematics of the experimental setup (Bergdahl et al., 2016).

Table 3
Numerical model parameters used to simulate the experimental setup.

Length of cable, L [m]	33
Mass of cable per unit of length, m_c [kg/m]	0.0818
Equivalent cable diameter, d_c [m]	0.0022
Cable density, ρ_c [kg/m³]	7800
Axial stiffness, EA_c [N]	10000
Tangential drag coefficient, C_{D_t} [–]	0.5
Normal drag coefficient, C_{D_n} [–]	2.5
Tangential added mass coefficient, C_{a_t} [–]	0
Normal added mass coefficient, C_{a_n} [–]	3.8
Ground stiffness per unit of length, k_g [GPa/m]	3
Ground damping, ξ_g [–]	1
Ground friction coefficient, μ_g [–]	0.3
Friction velocity, v_μ [–]	0.01

(Bergdahl et al., 2016). A brief overview of the test campaign is given below.

A catenary mooring chain of 33 m is placed in a 3 m deep water tank. The cable is fixed by a weight on the ground on one end. The other end is connected to a rotating sheave installed slightly above the water level and spun at a defined rotational speed. At the same time, a load cell measures the tensile force, as shown in Fig. 6.

The tested rotational periods are $\tau = 1.25$ s and $\tau = 3.50$ s. For $\tau = 1.25$ s, the circular amplitude was changed between $0.075 - 0.2$ m, according with the available experimental data. A listing of the pertinent parameters concerning the experimental setup and utilized for the numerical model are presented in Table 3, including the material characteristics of the mooring line. A total of 250 nodes were used in the numerical discretization with a CFL = 0.05 for both cases.

The chain is modelled with bilinear axial stiffness, not allowing axial compression (negative strain). Therefore, if local negative strain values are obtained during the computations, the corresponding axial stiffness value switches to zero. Moreover, the afloat sections of the cable are taken into account by modifying the source term.

In Fig. 7, the tension magnitude time-series for a circular motion amplitude equal to 0.2 m and both rotational periods is presented, comparing the numerical and experimental results. For $\tau = 1.25$ s (Fig. 7

a), despite the numerical model slightly underpredicting the maximum tension value, the global agreement is sound, particularly near the peak tension cycle behaviour. When the tension is close to zero (slacking regime), the numerical tension displays large fluctuating values, which are also observed in the experimental results, but at a smaller scale. However, this behaviour is primarily numerical and is derived from the seabed model implemented (linear spring–damper). The local strain gradients on ground nodes induce artificial tension oscillations (Low et al., 2018). A finer discretization in time and space of the touchdown point might alleviate this effect (Low et al., 2019). Moreover, during the upstroke part of the motion, the behaviour of the tension is well-captured, particularly the tension recoil before the peak. As mentioned in (Palm et al., 2017), there is a snap load formation during the slacking phase. The resultant wave is reflected at the upper end of the cable, thus leading to an enhanced spike in tension. The minor difference in
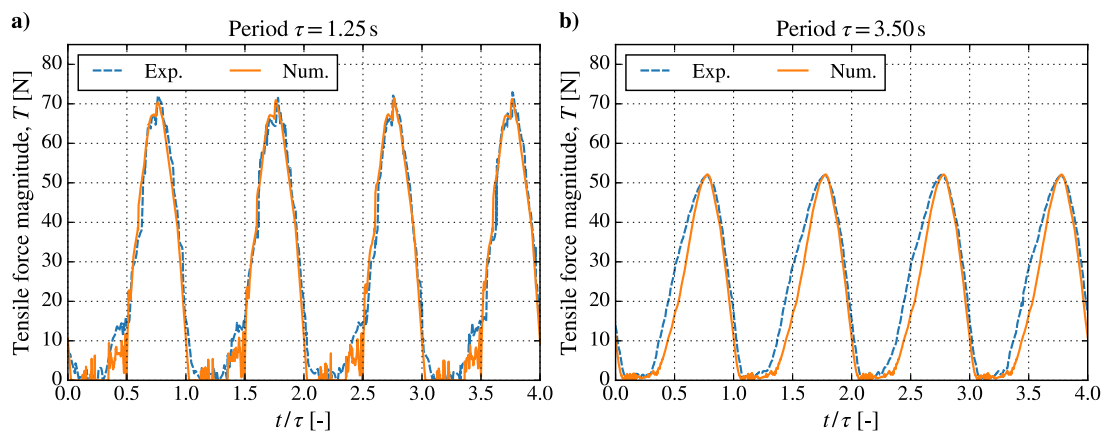
Fig. 7. Comparison of numerical and experimental tensile force measured at the upper-end for the test case with (a) period $\tau = 1.25$ s and (b) period $\tau = 3.50$ s and circular radius of 0.2 m.

Table 4
Maximum mean tensile force ($T_{\max}$) for a rotational period $\tau = 1.25$ s and different sheave radiuses.

$T_{\max}$ [N]	Circular motion radius [m]				
	0.075	0.100	0.125	0.150	0.200
Exp.	42.5	46.8	54.1	60.4	70.3
Num.	39.8	48.1	52.6	57.9	70.6

the peak tension between the experimental and the numerical values, which are related to the snap load, can be owed to several factors associated with the numerical implementation, such as the ground model, thus difficulting the interpretation of current data. However, the mean maximum experimental force is very close the experimental one, see Table 4.

On the other hand, the results for $\tau = 3.50$ s exhibited in Fig. 7b are in reasonable agreement for the peak tension values but have a different ascending part of the curve in comparison with the experimental tension series. For the numerical tensile force, the upward part is abrupter, and the slacking interval is more extended and includes high-frequency content. This loss in tension accuracy most likely derives from the source term effect on the solution. This term is evaluated based on each cell value. For $\tau = 3.50$ s the solution is smoother and the effect of this term is more pronounced. Therefore, the numerical scheme might not accurately reflect tension changes across the entire domain. In the shorter period, the presence of snap loads and sea bottom effects promotes highly transient responses, and the numerical flux term of the equations masks that influence. The aforementioned argument is a limitation of the current method for smooth solutions since it introduces a different tension behaviour compared to the experimental one.

Finally, complementary results are presented in Table 4 for the numerical maximum tensile forces (averaged over multiple period samples) under different circular motion radii and for a rotational period $\tau = 1.25$ s. The experimental values are added for comparison; generally, they are congruent over the entire range with no distinct under- or over-predictions tendencies.

4. Conclusions

Various numerical methods can simulate mooring cables, but few are targeted to calculate snap loads. In this regard, a Godunov-type finite-volume method (central-upwind scheme) was devised for resolving the numerical flux term of the hyperbolic equations of motion of a single mooring cable in a conservative form. This new approach enjoys the main advantage of (weak) finite-volume formulations, thus allowing discontinuous solutions in the tension, characteristic of snap loading regimes. The numerical model is formulated in a semi-discretized

state and evolved in time using the third-order strong stability preserving Runge–Kutta. The generalized minmod limiter was used to ensure TVD conditions. The boundary conditions were implemented using ghost cells.

The numerical model was evaluated against three different validation cases. Comparison with the analytical solutions demonstrated second-order spatial accuracy and accurate shock-capturing properties. The final validation case consisted of experimental results concerning a single catenary mooring line under slack conditions. The numerical results showed a good agreement with the experimental values, only slightly underpredicting the maximum tension peaks. Several factors can explain this difference, mainly concerning the numerical setup. For instance, the seabed model is expected to have a considerable influence on the simulation since the peak snap load is a reflection at the fairlead of a discontinuity appearing during the slack period. Additionally, high-frequency oscillations appear during this phase.

The proposed finite-volume method provides a more straightforward and practical approach than current codes available in the literature for modelling snap loads on perfectly flexible cables. This scheme does not use a Riemann solver; the only information required at cell interfaces are the local wave speeds. Currently, the applied scheme employs a linear function for the reconstruction step. Therefore, a fine grid is needed to handle smooth solutions. Increasing the polynomial degree for finite-volume schemes is challenging since a wider stencil is required. Additionally, an improved source-term treatment may increase the accuracy of the results. One approach is moving source terms into the flux using appropriate discretization procedures.

The suitability, advantages and limitations of this method are successfully demonstrated in this paper. At the same time, more conditions should be tested and compared with experimental data, and that is the focus of future work. Further improvements to the numerical model are envisioned. Examples include mesh refinement methodologies and nonlinear limiter switches between smooth and non-smooth solutions to increase spatial accuracy and decrease the computational cost.

CRediT authorship contribution statement

A.F.L. Governo: Conceptualization, Investigation, Methodology, Software, Data curation, Writing – original draft. **J.C.C. Henriques:** Conceptualization, Supervision, Visualization, Writing – review & editing, Funding acquisition. **L.M.C. Gato:** Conceptualization, Supervision, Resources, Writing – review & editing.

Declaration of competing interest

The authors declare that they have no known competing financial interests or personal relationships that could have appeared to influence the work reported in this paper.

Data availability

Data will be made available on request.

Acknowledgements

This research was partially supported by the Portuguese Foundation for Science and Technology - FCT, through IDMEC, under LAETA, project UIDB/50022/2020. The first author was supported by FCT, Portugal grant no. DFA/BD/07315/2021.

References

Aamo, O.M., Fossen, T.I., 2000. Finite element modelling of mooring lines. Math. Comput. Simulation 53 (4), 415–422. http://dx.doi.org/10.1016/S0378-4754(00)00235-4.

Aamo, O.M., Fossen, T.I., 2001. Finite element modelling of moored vessels. Math. Comput. Model. Dyn. Syst. 7 (1), 47–75. http://dx.doi.org/10.1076/mcmd.7.1.47.3632.

Aranha, J.A.P., Pinto, M.O., 2001. Dynamic tension in risers and mooring lines: An algebraic approximation for harmonic excitation. Appl. Ocean Res. 23 (2), 63–81. http://dx.doi.org/10.1016/S0141-1187(01)00008-6.

Azcona, J., Munduate, X., González, L., Nygaard, T.A., 2017. Experimental validation of a dynamic mooring lines code with tension and motion measurements of a submerged chain. Ocean Eng. 129, 415–427. http://dx.doi.org/10.1016/j.oceaneng.2016.10.051.

Bergdahl, L., Palm, J., Eskilsson, C., Lindahl, J., 2016. Dynamically scaled model experiment of a mooring cable. J. Mar. Sci. Eng. 4 (1), http://dx.doi.org/10.3390/jmse4010005.

Chen, L., Basu, B., Nielsen, S.R.K., 2018. A coupled finite difference mooring dynamics model for floating offshore wind turbine application. Ocean Eng. 162, 304–315. http://dx.doi.org/10.1016/j.oceaneng.2018.05.001.

Cristescu, N., 2007. Dynamic Plasticity. In: North-Holland series in Applied Mathematics and Mechanics, World Scientific.

Davidson, J., Ringwood, J.V., 2017. Mathematical modelling of mooring systems for wave energy converters - A review. Energies 10 (5), http://dx.doi.org/10.3390/en10050666.

Gobat, J., Grosenbaugh, M., 2001. Dynamics in the touchdown region of catenary moorings. Int. J. Offshore Polar Eng. 4 (11).

Goeller, J.E., Laura, P.A., 1971. Analytical and experimental study of the dynamic response of segmented cable systems. J. Sound Vib. 18 (3), 311–324. http://dx.doi.org/10.1016/0022-460X(71)90704-8.

Greiner, W., 2009. Classical Mechanics: Systems of Particles and Hamiltonian Dynamics. Springer Berlin Heidelberg.

Hann, M., 1995. Statics and dynamics of multi-cable systems for submersibles. Mar. Struct. 8 (5), 555–583, Moored and Tethered Structures. http://dx.doi.org/10.1016/0951-8339(95)97309-V.

Harnois, V., 2014. Analysis of Highly Dynamic Mooring Systems: Peak Mooring Loads in Realistic Sea Conditions (Ph.D. Thesis). College of Engineering, Mathematics and Physical Sciences, University of Exeter.

Hennessey, C.M., Pearson, N.J., Plaut, R.H., 2005. Experimental snap loading of synthetic ropes. Shock Vib. 12, 163–175. http://dx.doi.org/10.1155/2005/734345.

Hou, T.Y., Floch, P.L., 1994. Why nonconservative schemes converge to wrong solutions: error analysis. Math. Comp. 62, 497–530. http://dx.doi.org/10.2307/2153520.

Hover, F.S., 1997. Simulation of stiff massless tethers. Ocean Eng. 24 (8), 765–783. http://dx.doi.org/10.1016/S0029-8018(96)00038-8.

Hsu, W., Thiagarajan, K.P., Hall, M., MacNicoll, M., Akers, R., 2014. Snap loads on mooring lines of a floating offshore wind turbine structure. In: Proc. International Conference on Offshore Mechanics and Arctic Engineering, Volume 9A: Ocean Renewable Energy. http://dx.doi.org/10.1115/OMAE2014-23587.

Hsu, W., Thiagarajan, K.P., Manuel, L., 2017. Extreme mooring tensions due to snap loads on a floating offshore wind turbine system. Mar. Struct. 55, 182–199. http://dx.doi.org/10.1016/j.marstruc.2017.05.005.

Huang, S., Vassalos, D., 1993. A numerical method for predicting snap loading of marine cables. Appl. Ocean Res. 15 (4), 235–242. http://dx.doi.org/10.1016/0141-1187(93)90012-M.

Johanning, L., Smith, G.H., Wolfram, J., 2006. Mooring design approach for wave energy converters. Proc. Inst. Mech. Eng. M 220 (4), 159–174. http://dx.doi.org/10.1243/14750902JEME54.

Koh, C.G., Zhang, Y., Quek, S.T., 1999. Low-tension cable dynamics: Numerical and experimental studies. J. Eng. Mech. 125 (3), 347–354. http://dx.doi.org/10.1061/(ASCE)0733-9399(1999)125:3(347).

Kurganov, A., Noelle, S., Petrova, G., 2001. Semidiscrete central-upwind schemes for hyperbolic conservation laws and Hamilton–Jacobi equations. SIAM J. Sci. Comput. 23 (3), 707–740. http://dx.doi.org/10.1137/S1064827500373413.

Kurganov, A., Tadmor, E., 2000. New high-resolution central schemes for nonlinear conservation laws and convection–diffusion equations. J. Comput. Phys. 160 (1), 241–282. http://dx.doi.org/10.1006/jcph.2000.6459.

Kvitrud, A., 2014. Lessons learned from Norwegian mooring line failures 2010–2013. In: Proc. International Conference on Offshore Mechanics and Arctic Engineering, Volume 4A: Structures, Safety and Reliability. V04AT02A005. http://dx.doi.org/10.1115/OMAE2014-23095.

Lax, P.D., 1954. Weak solutions of nonlinear hyperbolic equations and their numerical computation. Comm. Pure Appl. Math. 7 (1), 159–193. http://dx.doi.org/10.1002/cpa.3160070112.

Lax, P., Wendroff, B., 1960. Systems of conservation laws. Comm. Pure Appl. Math. 13 (2), 217–237. http://dx.doi.org/10.1002/cpa.3160130205.

LeVeque, R.J., 1990. Numerical Methods for Conservation Laws, first ed. Birkhäuser Basel, http://dx.doi.org/10.1007/978-3-0348-5116-9.

Liu, F.C., 1973. Snap loads in lifting and mooring cable systems induced by surface wave conditions. Technical Note N-1228. Naval Civil Engineering Laboratory, Port Hueneme, CA.

Low, C.M., Ng, E.Y., Narasimalu, S., Lin, F., Kim, Y., 2018. Numerical modelling of seabed impact effects on chain and small diameter mooring cables. Appl. Ocean Res. 80, 248–277. http://dx.doi.org/10.1016/j.apor.2018.09.010.

Low, C.M., Yinkwee Ng, E., Narasimalu, S., Chua, K.H., Kim, Y., 2019. Adaptive discretisation and dual-rate time-stepping of mooring cable dynamics. Ocean Eng. 188, 106275. http://dx.doi.org/10.1016/j.oceaneng.2019.106275.

Ma, K., Shu, H., Smedley, P., L'Hostis, D., Duggal, A., 2013. A historical review on integrity issues of permanent mooring systems. In: Proc. OTC Offshore Technology Conference. http://dx.doi.org/10.4043/24025-MS.

Masciola, M., Robertson, A., Jonkman, J., Coulling, A., Goupee, A., 2013. Assessment of the importance of mooring dynamics on the global response of the DeepCwind floating semisubmersible offshore wind turbine. Proceedings of the International Offshore and Polar Engineering Conference 359–368.

Niedzwecki, J.M., Thampi, S.K., 1991. Snap loading of marine cable systems. Appl. Ocean Res. 13 (1), 2–11. http://dx.doi.org/10.1016/S0141-1187(05)80035-5.

Palm, J., Eskilsson, C., 2020. Influence of bending stiffness on snap loads in marine cables: A study using a high-order Discontinuous Galerkin method. J. Mar. Sci. Eng. 8 (10), http://dx.doi.org/10.3390/jmse8100795.

Palm, J., Eskilsson, C., Bergdahl, L., 2017. An hp-adaptive Discontinuous Galerkin method for modelling snap loads in mooring cables. Ocean Eng. 144, 266–276. http://dx.doi.org/10.1016/j.oceaneng.2017.08.041.

Qiao, D., Haider, R., Yan, J., Ning, D., Li, B., 2020a. Review of wave energy converter and design of mooring system. Sustainability 12 (19), http://dx.doi.org/10.3390/su12198251.

Qiao, D., Yan, J., Liang, H., Ning, D., Li, B., Ou, J., 2020b. Analysis on snap load characteristics of mooring line in slack-taut process. Ocean Eng. 196, 106807. http://dx.doi.org/10.1016/j.oceaneng.2019.106807.

Savin, A., Svensson, O., Leijon, M., 2012. Azimuth-inclination angles and snatch load on a tight mooring system. Ocean Eng. 40, 40–49. http://dx.doi.org/10.1016/j.oceaneng.2011.12.007.

Suhara, T., Koterayama, W., Tasai, F., Hiyama, H., Sao, K., Watanabe, K., 1981. Dynamic behavior and tension of oscillating mooring chain. In: Proc. OTC Offshore Technology Conference. http://dx.doi.org/10.4043/4053-MS.

Tjavaras, A., 1996. The Dynamics of Highly Extensible Cables (Ph.D. Thesis). Massachusetts Institute of Technology, Dept. of Ocean Engineering.

Triantafyllou, M.S., 1999. Chapter 6 - Cable dynamics for offshore application. In: Herbich, J.B., Ansari, K.A., Chakrabarti, S.K., et al. (Eds.), Developments in Offshore Engineering. Gulf Professional Publishing, Houston, pp. 256–294. http://dx.doi.org/10.1016/B978-088415380-1/50025-X.

Triantafyllou, M.S., Howell, C.T., 1994. Dynamic response of cables under negative tension: An ill-posed problem. J. Sound Vib. 173 (4), 433–447. http://dx.doi.org/10.1006/jsvi.1994.1239.

Vassalos, D., Huang, S., 1996. Dynamics of small-sagged taut-slack marine cables. Comput. Struct. 58 (3), 557–562. http://dx.doi.org/10.1016/0045-7949(95)00159-E.

Vassalos, D., Kourouklis, A., 1998. An Experimental, Theoretical and Full-Scale Investigation on the Snap Loading of Marine Cables. Offshore Technology Report OTH 558, Department of Ship and Marine Technology University of Strathclyde, pp. 1–181.